Spectroscopic and electrokinetic evidence for a bifunctional mechanism of the oxygen evolution reaction

Lichen Bai‡, Seunghwa Lee‡, Xile Hu*

Laboratory of Inorganic Synthesis and Catalysis, Institute of Chemical Sciences and Engineering, École Polytechnique Fédérale de Lausanne (EPFL), ISIC-LSCI, 1015 Lausanne, Switzerland

ABSTRACT: The oxygen evolution reaction (OER) is an essential anodic reaction in many energy storage processes. OER is most often proposed to occur via a mechanism involving four consecutive proton-coupled electron transfer (PCET) steps, which imposes a performance limit due to the scaling relationship of various oxygen intermediates. A bifunctional OER mechanism, in which the energetically demanding step of the attack of hydroxide on a metal oxo unit is facilitated by a hydrogen atom transfer to a second site, has the potential to circumvent the scaling relationship. However, the bifunctional mechanism has hitherto only been supported by theoretical computations. Here we describe an operando Raman spectroscopic and electrokinetic study of two highly active OER catalysts, FeOOH-NiOOH and NiFe layered double hydroxide (LDH). The data support two distinct mechanisms for the two catalysts: FeOOH-NiOOH operates by a bifunctional mechanism where the rate-determining O-O bond forming step is the OH^- attack on a Fe=O coupled with a hydrogen atom transfer to a Ni^{III}-O site, whereas NiFe LDH operates by a conventional mechanism of four consecutive PCET steps. The experimental validation of the bifunctional mechanism enhances the understanding of OER catalysts.

1. Introduction

The oxygen evolution reaction (OER) is an essential anodic reaction for many cathodic electrochemical reactions, such as hydrogen evolution reaction (HER), CO_2 reduction reaction (CRR), and N_2 reduction reaction (NRR), which may be used to generate renewable fuels and valuable chemicals.[1-2] An electrocatalyst, typically a metal oxide or oxyhydroxide, is required for OER to occur at a conceivable rate.[3-5] The OER involves four electrons and protons, rending it mechanistically complex.[3, 5-7] For OER catalyzed by metal oxides and oxyhydroxides, the most commonly assumed mechanism involves four consecutive proton-coupled electron transfer, where the O-O bond forming step is nucleophile attack of water or hydroxide on a metal oxo species (Scheme 1a).[6, 8] DFT computations revealed a scaling relationship between the adsorption energies of OH*, O*, and OOH*.[8-9] In particular, the difference of the adsorption energies of *OH and *OOH is always 3.2 eV for nearly all metal oxides. This scaling relationship poses an upper limit on the performance of OER catalysts, which has a theoretical overpotential of about 0.4 eV.[8-9]

To break the performance limit imposed by the scaling relationship, a change of catalytic mechanism is required.[10-11] An alternative mechanism involves the combination of two metal oxo species as the O-O bond forming step (Scheme 1b). Although there is theoretical debate in whether this O-O bond forming step is kinetically favourable compared to the nucleophilic attack step,[12-13] electrokinetic studies seem to support such a mechanism in a number of systems.[14-16] In addition to these two conventional mechanisms, a third-type, so-called "bifunctional" mechanism has recently been proposed.[11, 17-19] This mechanism involves two catalytic sites, often based on two different metal ions, which work in a cooperative manner (Scheme 1c). One site provides the electrophilic M=O entity, while the other side provides a hydrogen atom acceptor (A). Although the direct nucleophilic attack of an OH^- on the M=O to form the M-

OOH intermediate is energetically too unfavourable, a concerted hydrogen atom transfer to the neighbouring acceptor significantly lowers the energetics.

Until now, the bifunctional mechanism is supported by DFT computations only.[11, 17-19] In a previous study, we developed an unconventional iron nickel catalyst, FeOOH-NiOOH, that was significantly more active than Ni-Fe oxyhydroxides and related layered double hydroxides (NiFeO$_x$H$_y$ and NiFe LDH), which were the benchmark OER catalyst in alkaline medium.[19] Operando X-ray absorption spectroscopy revealed the catalyst as nanoclusters of γ-FeOOH covalently linked to a γ-NiOOH support. According to DFT computations, this structure could enable a bifunctional mechanism where the O-O bond forming step is a nucleophilic attack of OH^- on a Fe=O moiety coupled with a concerted hydrogen atom transfer to a nearby terrace O site on the γ-NiOOH support. Here we present in-situ Raman spectroscopy and electrokinetic data that support this mechanism. The experimental validation of the bifunctional mechanism stimulates both the mechanistic understanding and the design principles of OER catalysts.

(a)

(b)

(c)
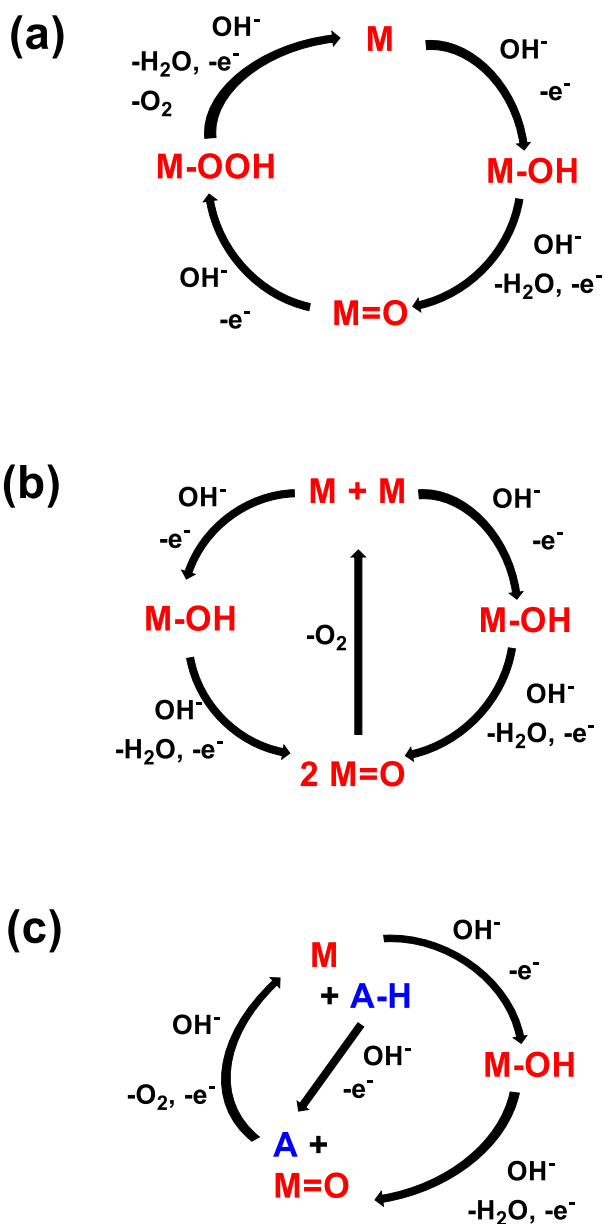
Scheme 1. Three OER mechanisms. (a) A conventional mechanism involving four consecutive proton-coupled electron transfers; (b) A conventional mechanism involving combination of two metal oxo species as the O-O bond forming step; (c) An unconventional 'bifunctional' mechanism. M represents an active metal center, A represents a hydrogen atom acceptor.

2. Results

2.1 Compositions and activity of catalysts

As described previously, FeOOH-NiOOH was prepared by dipping a clean nickel form (NF) in a solution of $FeCl_3$, drying in air at 80 °C, followed by anodic activation in a Fe-containing KOH.[19] While previously we assigned the support as pure NiOOH, we found in the present study that some Fe ions were incorporated in the lattice of NiOOH, which resulted in a positive shift of the $Ni(OH)_2$/NiOOH oxidation potential[20-22] during the formation of FeOOH-NiOOH (Figure S1). The distribution of Fe was not uniform, according to transmission electron microscopy (TEM), and energy dispersed X-ray (EDX) mapping (Figure S2 and S3). Because Fe-doped NiOOH is an active OER catalyst,[20-22] to probe the possible influences of the Fe doping in the NiOOH support in the activity and mechanism, we chose NiFe LDH as a reference sample. Previous studies suggested the structure of NiFe LDH is the active motif of Fe-doped NiOOH.[20, 23] Additionally, DFT computations suggested OER occurred via four consecutive PCET steps on this conventional NiFe oxyhydroxide catalyst.[23-25] The NiFe LDH was prepared according to literature.[26] The compound was characterized by powdered X-ray diffraction (PXRD), transmission electron microscopy (TEM), and energy dispersed X-ray (EDX) mapping (Figure S4 and S5). The Ni and Fe ions appeared to be uniformly distributed in NiFe LDH (Figure S5), and the Fe content was about 22%.
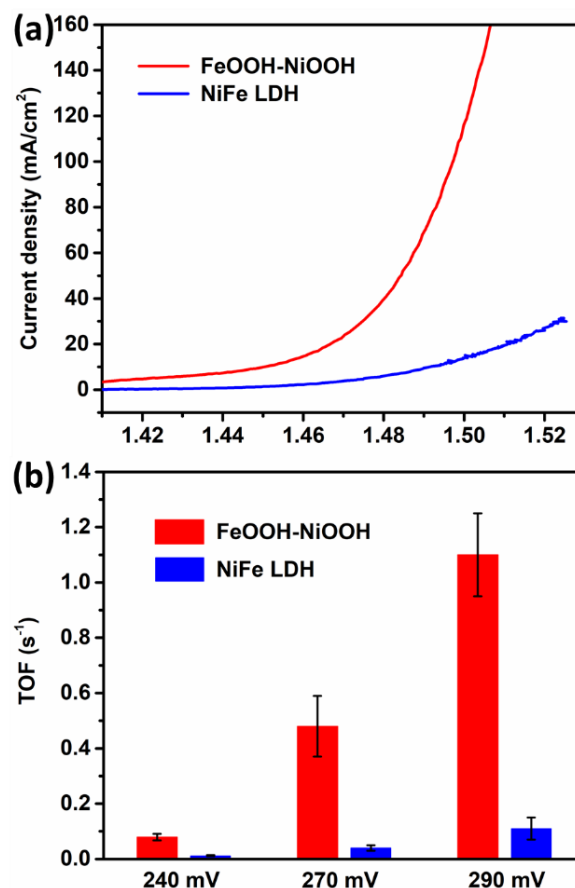

Figure 1. Electrocatalytic activity. (a) LSV curves of FeOOH-NiOOH (red) and NiFe LDH (blue) in 1 M KOH. (b) Comparison of TOFs of FeOOH-NiOOH (red) and NiFe LDH (blue) at various overpotentials.

We compared the activity of FeOOH-NiOOH and NiFe LDH with similar Fe loadings (Figure S6). To avoid the formation of some FeOOH-NiOOH on NF during OER test,[19] the activity of NiFe LDH was tested on a carbon-cloth (CC) electrode. Both catalysts were activated by multiple cyclic voltammetric (CV) scans (Figure S1a, S7). The activation of FeOOH-NiOOH was related to the incorporation of Fe ions and formation of FeOOH

as reported previously.[19] The activation of NiFe LDH was related to a morphology change that increased the surface area, which was indicated by the increase of areas of the oxidation of $Ni(OH)_2$ to NiOOH (Figure S7). Moreover, TEM and HAADF-STEM images (Figure S4b, S5, S8 and S9) showed that the initial, large lamellar structure cracked into small layers upon activation, while the Fe/(Ni+Fe) ratio remained unchanged (Figure S5e and S9e). According to linear sweep voltammetry (LSV) data (Figure 1a and S10), the FeOOH-NiOOH is significantly more active than NiFe LDH, both in apparent geometric activity (Figure 1a) and in electrochemical surface area (ECSA)-averaged activity (Figure S10). The turnover frequencies (TOFs) were also compared assuming a bimetallic Ni-Fe active site for both catalysts (Figure 1b). The FeOOH-NiOOH has TOFs that are about 10 times higher than those of NiFe LDH. These data indicate a difference in the active sites of FeOOH-NiOOH and NiFe LDH, and confirm that the Fe-doped NiOOH support had no noticeable contribution to the measured activity of FeOOH-NiOOH.
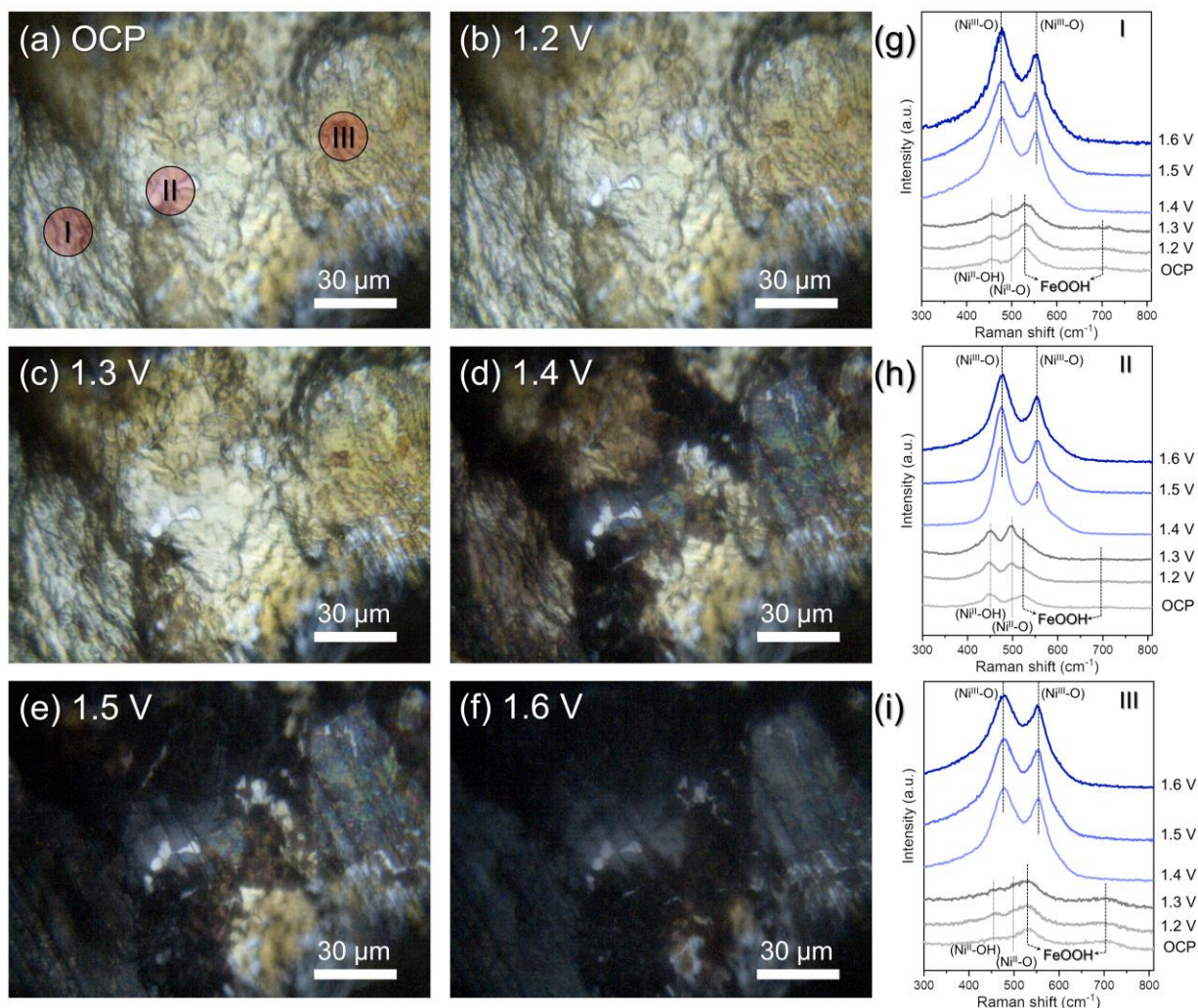

Figure 2. Operando Raman spectroscopic analysis. (a-f) Optical microscopy images of FeOOH-NiOOH at given potentials and (g-i) the corresponding operando Raman spectra obtained from three different spots as indicated in the (a).

2.2. Operando Raman spectroscopic data

2.2.1 Spectral features

Figure 2 shows operando Raman optical microscopy images and spectra of FeOOH-NiOOH, recorded from the open circuit potential (OCP) to 1.6 V (vs. RHE) with an interval of 0.1 V. Due to FeOOH, the surface looks brownish-yellow at OCP compared with bare NF (Figure S11), which is silver-white.[19, 27] The microscope objective collected Raman signals from three different beam spots (I, II, and III in Figure 2a). The surface gradually turned into black from 1.4 V (Figure 2b-f), indicative of the formation of Fe-doped NiOOH support.[28-29] The potential-dependent Raman spectra vary at three different spots of the surface (Figure 2g-i), indicating a surface heterogeneity. Indeed TEM and EDX mapping images (Figure S2 and S3) showed that Fe ions were not uniformly distributed on the surface. Consistent with previous XAS results,[19] surface γ-FeOOH species were identified by two main Raman bands at 526 cm^{-1} and 690 cm^{-1} (Figure 2g-i and S12).[19, 30-31] At 1.4 V and above, two strong Raman bands at around 480 and 560 cm^{-1} were observed (Figure 2g-i). These two bands correspond to the Ni-O bending and stretching vibrations of NiOOH, respectively.[22, 32-35] Their appearance indicated the presence of NiOOH at these potentials, again consistent with previous XAS data.[19] At the three chosen spots on the surface, the relative intensities of the 480 cm^{-1} and 560 cm^{-1} bands (I_B/I_S) and the half-widths of the two

bands vary, indicating different local environments around the Ni-O bonds. Fe-incorporation into NiOOH causes structural defects and disorder of lattice, which leads to a lower I_B/I_S.[22, 32, 35] Accordingly, the amount of Fe dopant in the NiOOH at the three spots follows the order of: III > I > II. A broad band in the frequency range of 900 to 1150 cm^{-1}, previously attributed to Ni-OO$^-$,[32-34, 36] was observed from 1.375 V (Figure S13a).

The Operando Raman spectra collected of NiFe LDH from OCP to 1.5 V (Figure S13b) show no spectral features corresponding to γ-FeOOH. Compared to Ni LDH and pure NF, NiFe LDH exhibits a peak corresponding to Ni^{II}-O vibration at around 530 cm^{-1} but not 500 cm^{-1}, which originates from the structural disorder induced by Fe doping. (Figure S13b and S14).[30, 35, 37] The two Raman bands of Ni^{III}-O (from NiOOH) began to grow from 1.375 V and the growth was completed at around 1.45 V (Figure S13b). The broad band in higher frequency range of 900 to 1150 cm^{-1}, due to Ni-OO$^-$,[32-34, 36] appeared from about 1.4 V.(Figure S13b).
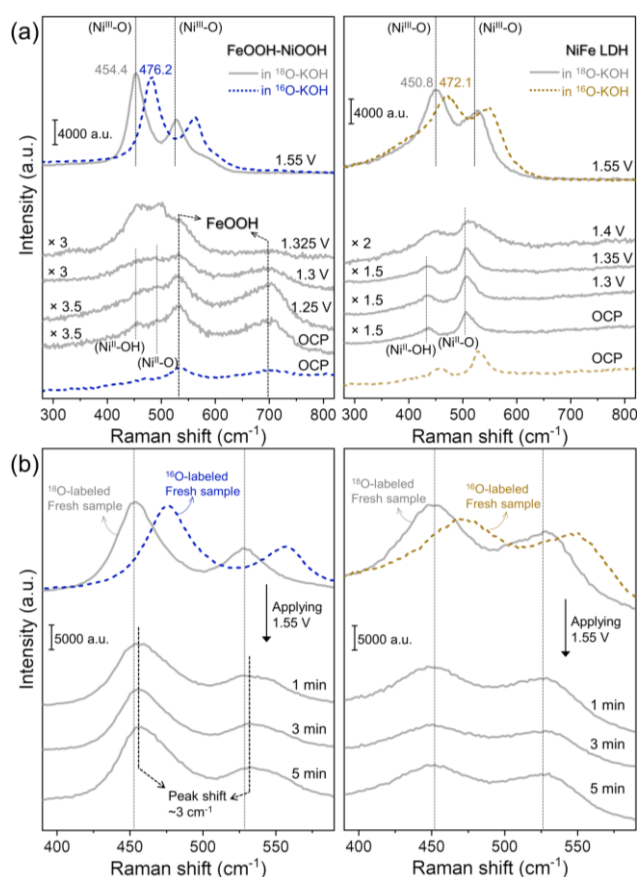

Figure 3. Operando Raman spectra of FeOOH-NiOOH (left column) and NiFe LDH (right column) obtained at various potentials for oxygen isotope labeling (a) in 1 M KOH-H$_2^{18}$O solution and (b) subsequent isotope exchange experiments. The ^{18}O-labeled samples were monitored at 1.55 V in 1 M KOH-H$_2^{16}$O solution. For ease of comparison of peak shift in between the two solutions, ^{16}O-labeled peaks of each sample are indicated respectively.

We compare directly the representative Raman spectra of FeOOH-NiOOH and NiFe LDH at OCP and 1.5 V (Figure S15). At OCP, Ni is mostly in the +2 oxidation state, and the Ni^{II}-O bands have low intensities (Figure S15, left). Accordingly, Raman bands due to FeOOH could be observed (Figure S15, left).

The presence of FeOOH in FeOOH-NiOOH, but not NiFe LDH, was obvious. At 1.5 V, NiOOH is formed where Ni is in the oxidation state of +3, and the Ni^{III}-O bands have high intensities (Figure S15, right). The I_B/I_S of NiFe LDH (1.18) was significantly lower than that of FeOOH-NiOOH (1.72), bare NF (1.91), and Ni LDH (2.2) (Figure S15 and S16), indicative of the highest structural disorder of NiFe LDH among the four samples. Because this NiFe LDH sample contains 20% whereas FeOOH-NiOOH has an Fe content of about 10% in some region (Figure S3), Raman spectra were also recorded for a NiFe LDH with 10% Fe (Figure S17, EDX mapping images and CVs of this catalyst are in Figure S18-S19). The I_B/I_s of NiFe LDH (10%Fe) was 1.33, again lower than that of FeOOH-NiOOH.

2.2.2 Oxygen isotope exchange experiments

We conducted ^{18}O isotope labeling and exchange experiments on FeOOH-NiOOH and NiFe LDH. The as-prepared, ^{16}O-labeled, samples were first immersed in a ^{18}O-KOH solution. For FeOOH-NiOOH at OCP to about 1.3 V, the peak of FeOOH remained at the same position whereas the peaks of Ni^{II}-O, Ni^{II}-OH appeared to be shifted, but the shift could not be quantified due to an overlap of peaks.(Figure 3a, left) For NiFe LDH same as reported previously,[32-33] the peaks of Ni^{II}-O, Ni^{II}-OH at OCP to about 1.35 V red-shifted by about 22 cm^{-1}, indicating the exchange of lattice ^{16}O with ^{18}O of the electrolyte (Figure 3a, right). Upon formation of NiOOH, and more obviously at 1.55 V, the Ni^{III}-O bands were observed at around 455 and 535 cm^{-1} for both FeOOH-NiOOH and NiFe LDH, red-shifted by about 22 cm^{-1} relative to those of ^{16}O-labeled samples. This shift indicates O isotope exchange. For FeOOH-NiOOH, the Raman peaks of γ-FeOOH did not shift during this process up to 1.325 V. At higher potentials the peaks were hidden by those of Ni^{III}-O bands. To probe whether lattice O in FeOOH was exchanged during OER, a FeOOH-NiOOH sample was first subjected to a ^{18}O-KOH solution at 1.55 V where OER was occurring, and then the Raman spectrum was collected at 1.25 V. Again the Raman peaks of γ-FeOOH remained at the same positions of a ^{16}O-labeled sample (Figure S20). Thus, the lattice oxygens of γ-FeOOH do not exchange with the electrolyte even under OER.

The ^{18}O-labeled samples of FeOOH-NiOOH and NiFe LDH were immediately placed back in a 1 M ^{16}O-KOH solution and potentiostatically charged at 1.55 V. For FeOOH-NiOOH, the peaks corresponding to Ni^{III}-O vibrational modes were shifted by about 3 cm^{-1} to high frequencies (Figure 3b, left). For NiFe LDH, no shift of peaks related to Ni^{III}-O was observed (Figure 3b, right). As a reference, a shift of 18 cm^{-1} was observed on bare NF (Figure S21).

2.3 Electrokinetic data

FeOOH-NiOOH exhibited a similar Tafel Slope of 38±2 mV/dec in 0.5 M to 2 M KOH (Figure 4a, S22a, Table S1). The potentials vs. Ag/AgCl (pH independent) at 10 mA/cm^2 linearly depended on the log of the concentration of hydroxyl ions (Figure 4b), with a slope of -74 mV/dec. The rate order of [OH$^-$] in 0.5-2 M KOH was determined according to Eq. 1.

$$\left(\frac{\partial \log j}{\partial \log [OH^-]} \right)_E = - \frac{\left(\frac{\partial E}{\partial \log [OH^-]} \right)_j}{\left(\frac{\partial E}{\partial \log j} \right)_{pH}} \qquad \text{Eq. 1}$$

The denominator of eq.1 is the Tafel slope and the numerator is the slope in Figure 4b. Accordingly, the order of [OH$^-$] was 1.8±0.1.

Similar analysis was performed for NiFe LDH (Figure 4c, 4d, S23a). The Tafel slopes of NiFe LDH are 42 to 48 mV/dec, depends on the concentration of hydroxyl ions (Figure 4c, Table S1). The Tafel slope decreased with increasing [OH⁻]. The Tafel slope in 2 M KOH is close to 40 mV/dec, similar to that of FeOOH-NiOOH. The potentials vs. Ag/AgCl (pH independent) at 1 mA/cm² linearly depended on the log of the concentration of hydroxyl ions (Figure 4d), with a slope of -80 mV/dec. According to Eq. 1, the rate order of [OH⁻] was also close to two.

The redox potentials of the precatalytic Ni(II)/Ni(III) shifted negatively by ca. 100 mV when the [OH⁻] increased by 10 fold, indicating a 3OH⁻/2e⁻ process (Figure S22b-c, S23b-c) for both FeOOH-NiOOH and NiFe LDH. The activity of NiFe LDH was very different in 1 M KOH, NaOH, LiOH (Figure S24a), indicating a cation effect. On the contrary, the cation effect was not obvious for FeOOH-NiOOH (Figure S24b).

The OER activity of FeOOH-NiOOH had an H/D isotope effect of 1.4 to 2.0, depending on the concentration of hydroxyl ions and the applied potential (Figure 4e, S25a, S26a). On the other hand, NiFe LDH had an H/D isotope effect of 2.0-2.4 (Figure 4f, S25b, S26b), and the isotope effect did not vary substantially at different potentials nor [OH⁻].
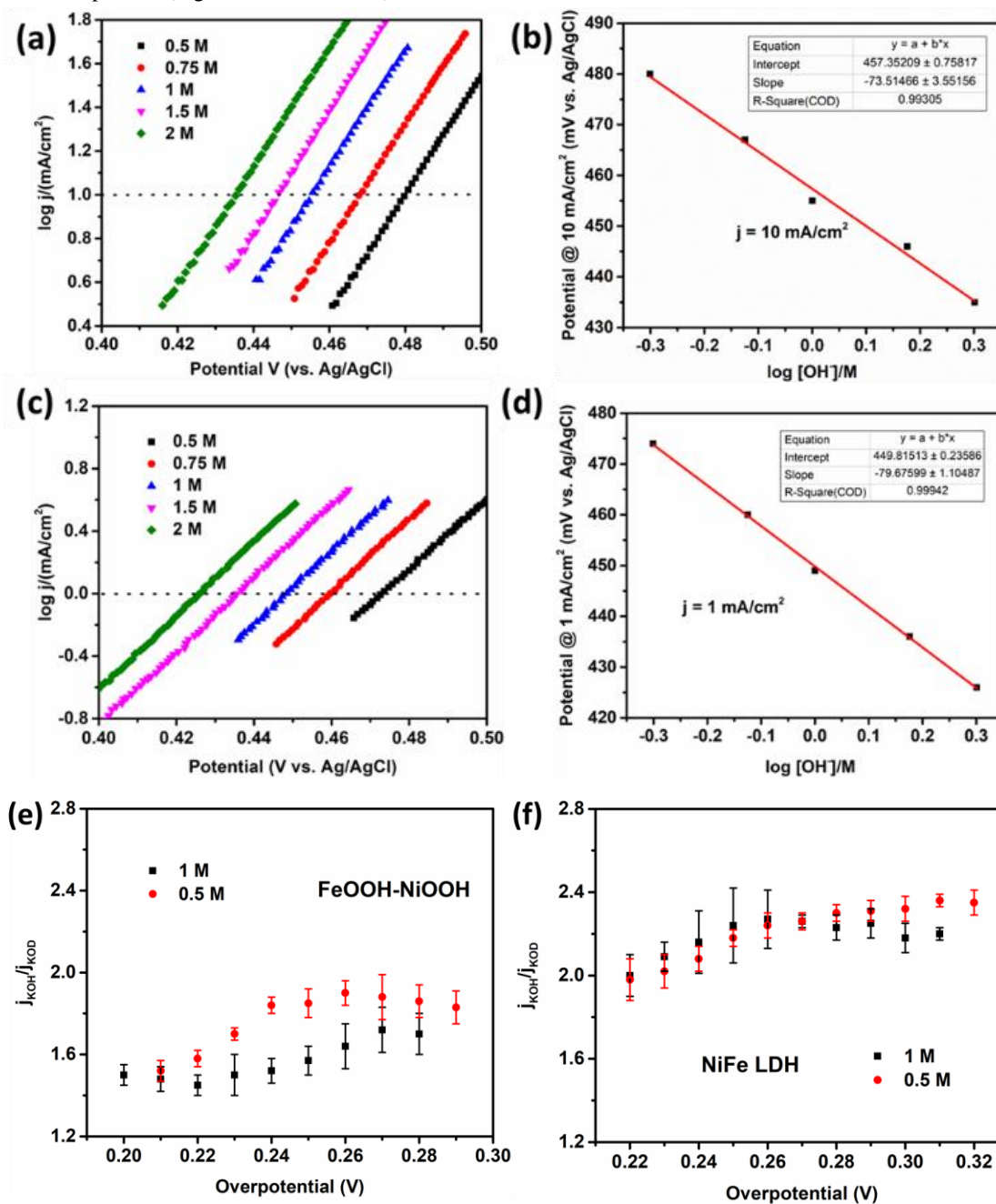

Figure 4. Electrokinetic analysis. (a) and (b) for FeOOH-NiOOH. (c) and (d) for NiFe-LDH. (a) and (c) The Tafel plots in different concentrations of KOH. The original LSVs are provided in SI. (b) and (d) The change of constant potential at a certain current density (10 mA/cm² for FeOOH-NiOOH and 1 mA/cm² for NiFe LDH) based on the logarithm of [OH⁻]. The linear fitting of the data points gives the $(\partial E/\partial \log [OH^-])_j$ values, as the slope of the fitting plot. (e-f) H/D isotope effect analysis (j_{KOH}/j_{KOD} versus overpotential). (e) NiFe LDH and (f) FeOOH-NiOOH. Electrolyte concentrations: 1 M (black), 0.5 M (red). The error bar and the average values were deduced from 3 independent measurements.

3. Discussion

3.1 Raman spectroscopic analysis

Operando Raman spectra revealed the presence of surface γ-FeOOH in FeOOH-NiOOH, but not in NiFe LDH. Otherwise the two catalysts have a similar component, Fe-doped γ-NiOOH. Bulk γ-FeOOH is a poor OER catalyst,[23, 38] whereas the surface γ-FeOOH here is responsible for remarkable OER activity (Figure 1, and S10). This difference suggests a mechanism that involves more than γ-FeOOH alone. The doping of Fe in NiOOH causes structural disorder in the lattice of NiOOH, which could be inferred by the I_B/I_S of the Raman spectra of NiOOH. [22, 32, 35] The lower structural disorder of FeOOH-NiOOH compared to NiFe LDH is consistent with most Fe ions being on the surface in FeOOH-NiOOH but in the bulk of NiFe LDH.

As reported previously,[32-33] the lattice O of NiOOH in NiFe LDH can exchange with O from the OH⁻ electrolyte. The exchange can occur without applying a potential when Ni is at the +2 oxidation state (as in $Ni(OH)_2$), but not when Ni is oxidized to +3 or above. The lattice O of NiOOH in FeOOH-NiOOH can also be exchanged at the Ni^{II} stage. Under OER potentials, a 3 cm⁻¹ isotopic shift of FeOOH-NiOOH indicates partial O exchange. Compared to bulk NF (18 cm⁻¹ shift), the exchange is about 16%. The different O exchange behavior reflects a mechanistic difference between FeOOH-NiOOH and NiFe LDH.

3.2. Electrokinetic analysis

3.2.1. Tafel slope and rate order

We employed a quasi-equilibrium model to describe the OER kinetics, in which the key steps are described by one pre-equilibrium step (PES) plus one rate-determining step (RDS).[39-40] The RDS limits the OER velocity while the PES determines the concentration of the resting states. The overall OER rate and catalytic behavior are controlled by both steps. The other steps are fast and do not restrict overall reaction rate. This model is suitable for catalysts in the intermediate applied overpotential (Tafel region), where the concentration of the resting state is not high (see Appendix 1, SI).

For the conventional mechanism involving four PCET steps (Scheme 1a), if the formation of M=O is the PES, and the nucleophilic attack of OH⁻ on a M=O is the RDS (Scheme 1a), the predicted Tafel slope is 40 mV/dec and the predicted rate order in [OH⁻] is two, assuming there is no charge transfer barrier.[40-41] For the bifunctional mechanism (Scheme 1c), if the formation of M=O is the PES, and the nucleophilic attack of OH⁻ on a M=O coupled with a hydrogen atom transfer is the RDS (Scheme 1c), the predicted Tafel slope is also 40 mV/dec and the predicted rate order in [OH⁻] is also two (Appendix 1, SI). The experimental values for both FeOOH-NiOOH and NiFe LDH, thus, agree with the predictions of both mechanisms. However, there are noticeable differences in the Tafel behaviors of FeOOH-NiOOH and NiFe LDH. The Tafel slopes of FeOOH-NiOOH is independent of [OH⁻]. In contrast, the Tafel slope of NiFe LDH decreases with increasing [OH⁻], suggesting a charge transfer barrier across the bulk film, which is more pronounced at lower [OH⁻] (for a detailed description, see SI, Appendix 1).[42-43] The absence of charge transfer barrier in FeOOH-NiOOH would be consistent with surface-dominated catalysis. The significant cation effect for NiFe LDH also indicates bulk sites are involved in OER,[44-46] although the origin of this effect is under debate.[44-46] The small cation effect observed for FeOOH-NiOOH is again consistent with surface catalysis.

3.2.2. H/D isotope effect

H/D exchange affects both thermodynamics and kinetics of PCET reactions.[47-48] Accordingly, both thermodynamic isotope effect (TIE) and the kinetic isotope effect (KIE) exist.[47-48] The TIE originates from a change in the reaction thermodynamics due to different vibrational zero-point energies (ZPEs) of bonds involving hydrogen and deuterium.[47, 49] In the present case, H/D TIE effect should be observed in PES involving proton transfer. On the other hand, H/D KIE originates from the different activation barriers caused by the differences of ZPEs between H- and and D-substituted analogues.[47-48, 50-51]. KIE is usually employed to probe the involvement of proton transfer in RDS.[47-48, 50-51] The combination of TIE and KIE leads to the overall observed isotope effect (IE).

For the conventional mechanism (Scheme 1a), there is direct proton transfer in the PES but not in RDS. Consequently, only TIE and secondary KIE are expected. Secondary KIE is typically below 1.3,[50, 52] so TIE would dominate. The data for NiFe LDH (H/D IE of 2.0-2.4) fit this model. The IE is roughly independent of applied potential, characteristic of TIE.[15, 49] Moreover, the IE is pH-independent, consistent with a PCET-type PES.[15, 49]

For the bifunctional mechanism, the direct proton/hydrogen transfer is involved in both PES and RDS (Scheme 1c), so that KIE becomes significant. In the Tafel region, the overall IE can be expressed as Eq. 2 (Appendix 2 of SI).[50]

$$IE = \frac{k_0}{k_0'}\exp\left(\frac{(\alpha_2 - \alpha_2')\eta F}{RT}\right) \qquad \text{(Eq. 2)}$$

k_0 and k_0' are the rate constants of H- and D-substituted reactants, respectively; α_2 and α_2' are the transfer coefficients of RDS for H- and D-substituted reactants; R, T, η, and F are universal gas constant, thermodynamic temperature, overpotential, Faradaic constant, respectively. Typically α_2 is bigger than α_2' due to a higher barrier of charge transfer after D-substitution.[50] In the Tafel region, k_0 and k_0', α_2 and α_2' can be considered potential-independent. Therefore, the observed IE should increase with increasing overpotential. Moreover, if the generation of the hydrogen atom acceptor is pH-dependent, the KIE is expected to depend on pH as well.[53] The data for FeOOH-NiOOH fit this model. The observed isotopic effect indeed increases with applied overpotential, and decreases with [OH⁻]. Note that the overall IE of FeOOH-NiOOH, dominated by KIE, is lower than that of NiFe LDH, dominated by TIE. Accordingly, the TIE of FeOOH-NiOOH is lower than that of NiFe LDH, reflecting a difference in the nature of M=O in these two catalysts. The KIE of FeOOH-NiOOH is rather small likely due to the internal hydrogen transfer in RDS. Previous literatures suggested internal hydrogen or proton acceptor could minimize the H/H⁺ transfer distance, significantly decreasing the H/D KIE.[54-55]

3.3. Catalytic cycle

Based on the above data, we propose a catalytic cycle for FeOOH-NiOOH (Figure 5a). The as-prepared catalyst A-I is composed of γ-FeOOH clusters covalently linked to a $Ni(OH)_2$ support, which is lightly doped by Fe. At about 1.35 V, the support is oxidized to NiOOH via a 3OH⁻/2e⁻ process. The process is best described by oxidation of a dimeric Ni^{II} unit into a dimeric Ni^{III} unit accompanied by the loss of three protons from coordinated water or OH⁻ groups (A-II). The Fe^{III} center in FeOOH then undergoes a PCET to form an electrophilic Fe(IV)=O center (A-III), which is the PES of the catalytic cycle. Consequently and in the RDS, the Fe(IV)=O center, an external

OH⁻, and the Ni^{III}-O moiety react in a concerted manner to give Fe^{II}-Ni^{II}-OH (A-IV), O₂ and an electron. Oxidations of Fe^{II} and Ni^{II} then regenerates the catalyst (A-II).
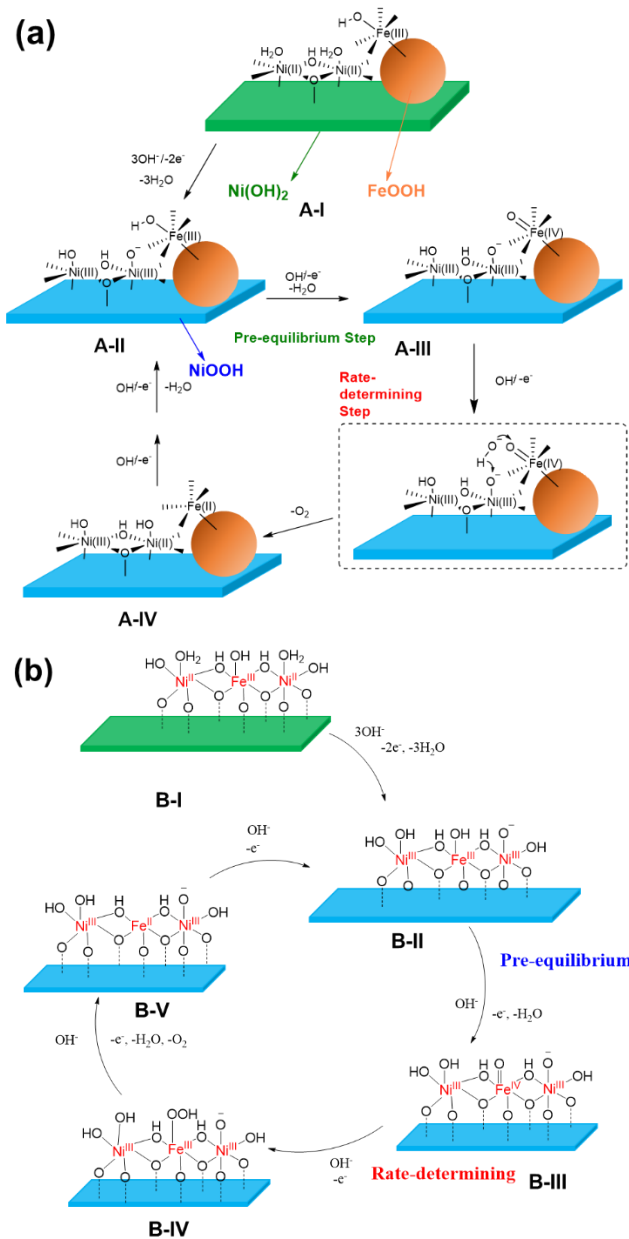

Figure 5. Proposed OER reaction mechanisms of (a) FeOOH-NiOOH. (b) NiFe LDH (assuming Fe is the catalytic center).

For NiFe LDH (Figure 5b), the as-prepared catalyst is comprised of Ni(OH)₂ doped by Fe^{III} ions (B-I). A 3OH⁻/2e⁻ process generates Fe-doped NiOOH (B-II). Although there are debates on whether Ni or Fe site serves as the site of O-O bond formation,[3, 23, 56] a dimeric Fe-O-Ni active site would agree with most data. The catalytic cycle proceeds via a PES to form a M=O (B-III, assuming M is Fe, but the same result is obtained when M is Ni), followed by a RDS of OH⁻ attack on M=O to give M-OOH (B-IV). A further PCET oxidation gives O₂ and M (B-V), which can then be oxidized back to the initial catalyst B-II. When M is Fe, the Fe ions shuffle between Fe^{II}, Fe^{III}, and Fe^{IV} while the Ni ions remain as Ni^{III} during catalysis. When M

is Ni, the Ni ions shuffle between Ni^{II}, Ni^{III}, and Ni^{IV} while the Fe ions remain as Fe^{III}.

The results from O isotope exchange experiments (Figure 3b) suggest the presence of transient Ni^{II} sites in FeOOH-NiOOH but not NiFe LDH during OER. About 16% of lattice O in FeOOH-NiOOH exchanges with OH⁻ under OER, but such an exchange is absent in NiFe LDH. It is known that at Ni^{II} the lattice O of Fe-doped NiOOH and NiFe LDH can exchange with O from OH⁻ electrolyte without applied potential, but at Ni^{III} and above, the exchange does not occur even under OER.[32-33] These results are consistent with FeOOH-NiOOH operating via the bifunctional mechanism (Figure 5a) where a Ni^{III}-O site accepts a hydrogen atom in the RDS to become a Ni^{II}-OH site. They are also consistent with NiFe LDH operating via the conventional mechanism (Figure 5b) where the redox changes occur at the Fe site.

4. Conclusion

Operando Raman spectroscopy and electrokinetic analysis were employed to study two active OER catalysts, FeOOH-NiOOH and NiFe LDH. Despite their similar chemical compositions, the two catalysts exhibit different electrochemical and spectroscopic features, which indicate that most Fe ions exist in surface γ-FeOOH clusters in FeOOH-NiOOH but they are doped in the lattice of Ni(OH)₂/NiOOH in NiFe LDH. This different results in a 10-fold higher OER activity of FeOOH-NiOOH compared to NiFe LDH. During OER, different O isotope exchange behaviors of the NiOOH component were observed for the two catalysts: about 16% of lattice O in FeOOH-NiOOH exchanged with the OH⁻ electrolyte whereas there was no exchange for NiFe LDH. These data suggest that Ni^{II} species are present in the catalytic cycle of FeOOH-NiOOH, but not NiFe LDH. The two catalysts exhibit similar Tafel slopes and rate orders in [OH⁻] under standard conditions. However, they have different H/D isotope effects. FeOOH-NiOOH has an IE of 1.4 to 2.0, which had a significant KIE component and depend on [OH⁻] and the overpotential. NiFe LDH had an IE of 2.0-2.4, which is mostly TIE and is independent of [OH⁻] and the overpotential. The spectroscopic and kinetic data support two distinct mechanisms for the two catalysts. FeOOH-NiOOH operates by a bifunctional mechanism where the rate-determining O-O bond forming step is the concerted OH⁻ attack on a Fe=O coupled with a hydrogen atom transfer to a Ni^{III}-O site. On the contrary, NiFe LDH operates by a conventional mechanism of four consecutive PCET steps, and the rate-determining O-O bond forming step is the attack of OH⁻ on a Fe=O unit.

The data describe here constitute the first experimental evidences for the bifunctional mechanism which has hitherto only computational supports. The superior activity of FeOOH-NiOOH demonstrates the potential of bifunctional catalysts to overcome the performance limit of conventional catalysts imposed by the scaling relationship. The bifunctional mechanism provide an opportunity to individually fine-tune two components of an OER catalyst for optimized activity, adding a new design principle. For example, analogous to the present FeOOH-NiOOH catalyst, the FeOOH component might be replaced by another material with a low energy barrier to form an electrophilic M=O unit, while the NiOOH component might be replaced by another hydrogen atom acceptor, including even organic materials.

5. Experimental Sections

5.1 Chemicals and the synthesis of the catalysts

KOD (30% in D_2O) is purchased from ABCR; ethanol (99.5%) is purchased from Fluka; 1 M KOH standard solution is purchased from Merck KGaA. All other chemicals were purchased from Sigma-Aldrich. The electrolytes were prepared by using ultra-pure water (18.2 MΩ/cm).

Pretreatment of nickel foam (NF) The NF was first cleaned by sonicating in acetone for 30 mins to remove the organic impurities. Then the NF was dried and dipped in 15% HCl for 30 mins with sonication. The electrode was washed by ultra-pure water and dried in room temperature. Noted that the electrode should be used within two hours, else the surface generated nickel hydroxide would decrease the adsorption ability of the catalysts (FeOOH).

Synthesis of FeOOH-NiOOH[19] A cleaned NF electrode was dipped in 10 mM $FeCl_3$ solution with stirring for 15 mins. After that, the electrode was directly dried in 75 °C oven over night. The FeOOH-NiOOH was formed during the drying period.

Synthesis of NiFe LDH (20% Fe) We used a method according to previous literature with modifications.[26] Typically, $Ni(NO_3)_2 \cdot 6H_2O$ (2.0 mmol, 582 mg), $Fe(NO_3)_3 \cdot 9H_2O$ (0.5 mmol, 202 mg), NH_4F (10 mmol, 371 mg) and urea (25 mmol, 1.50 g) were dissolved in H_2O (40 ml) with vigorous stirring. The mixed solution was stirred for 30 mins and then transferred to a 50 mL Teflon-lined stainless steel autoclave. The autoclave was heated at 120 °C for 16 h. After cooling down to room temperature, the yellowish solid was washed by ultrapure water for 3 times and ethanol for 1 time, and then naturally dried on a watch glass. If no special indication, the NiFe LDH samples mentioned in SI and main-text have 20% Fe content.

Synthesis of NiFe LDH (10% Fe) The synthetic procedure is a bit different to that of 20% Fe samples. Typically, the 40 mL DI water was degassed for 1h, before dissolving $Ni(NO_3)_2 \cdot 6H_2O$ (2.25 mmol, 654 mg), $FeSO_4 \cdot 7H_2O$ (0.25 mmol, 70 mg), NH_4F (10 mmol, 371 mg) and urea (25 mmol, 1.50 g). The mixed solution was stirred for 30 mins under nitrogen. Then the solution was sealed in a 50 mL Teflon-lined stainless steel autoclave. The autoclave was heated at 120 °C for 16 h. After cooling down to room temperature, the green solid was washed by ultrapure water for 3 times and ethanol for 1 time, and then naturally dried on a watch glass. The color of the solid will turn to yellow in the air, while the electrochemical property is not influenced by this color change.

Synthesis of Ni LDH The bulk Ni LDH was synthesized through a hydrothermal method.[57] 0.10 M of $Ni(NO_3)_2 \cdot 6H_2O$ and 0.15 M of urea were dissolved in 80 mL of deionized water that was already boiled to remove dissolved CO_2 in it. The mixed solution was sonicated for 30 mins to make it homogeneous. Then, the resulting solution was transferred to a 50 mL Teflon-lined stainless steel autoclave and heated at 190 °C for 48 h. The as-obtained green product was collected by centrifugation as it washed with ultrapure water for 3 times and ethanol for 1 time.

Synthesis of γ-FeOOH The material was synthesized according to previous literature with modifications.[19] Typically, 20 mL of 0.02 M $Fe(NO_3)_3$ solution was sealed in a glass container, which was then maintained at 75 °C for 24 h. After centrifuging and washing with water for 3 times and ethanol for 1 time, yellowish-brown powder was obtained as γ-FeOOH.

Preparation of Fe-free KOH The Fe-free KOH was prepared for Operando Raman experiments of pure NF and pure Ni LDH (see below). The Fe impurities in normal KOH solutions can be removed by treating with high-purity $Ni(OH)_2$.[20] In a clean 50 mL polypropylene centrifuge tube, 2 g of $Ni(NO_3)_2 \cdot 6H_2O$ (99.99%) was dissolved in 5 mL of ultrapure water. 20 mL of 1 M KOH solution was added to give a $Ni(OH)_2$ precipitate. The suspension was agitated and centrifuged, and the supernatant was decanted. The $Ni(OH)_2$ precipitate was washed with ultrapure water for three times by centrifugation. The solid was dispersed in 10 mL of 1 M KOH by centrifugation, and the supernatant was decanted. This solid was used as the Fe-absorber. The normal KOH solutions could be cleaned by adding to this $Ni(OH)_2$. The cleaning procedure involves dispersing $Ni(OH)_2$ in the KOH solution, mechanically agitated over-night, followed by at least 3 h of resting.

5.2 Characterizations

Powder X-ray diffraction (PXRD) measurements were carried out on an X'Pert Philips diffractometer in Bragg-Brentano geometry with monochromatic CuKα radiation (0.1541 nm) and a fast Si-PIN multi-strip detector. The step size was 0.02 degree s^{-1}. Transmission electron microscopy (TEM) was performed on an FEI Talos instrument that operated at 200 kV high tension. Energy dispersed X-ray (EDX) mapping was used for determining the distribution of the elemental compositions. The images were collected in HAADF-STEM (High-angle annular dark-field scanning transmission electron microscopy) mode and the mapping was performed in ESpirit software. Samples for TEM were prepared by drop-drying the samples from their diluted ethanol suspensions onto carbon-coated copper grids. Suspension of FeOOH-NiOOH was collected by sonicating the electrode in ethanol for 1h. ICP-AES (Inductively coupled plasma – Atomic Emission Spectroscopy) results were obtained by a NexIon 350 (Perkin Elmer) machine. All the samples were dissolved by ultra-pure nitric acid (65%, Merck KGaA) then diluted by 30 times.

Raman spectroscopic experiments were performed at a Raman spectroscopy (inVia confocal Raman microscope, Renishaw) with a 63x water immersion objective (Leica-Microsystems) for both operando and ex-situ analysis. A transparent Teflon film (0.001 in thickness, McMaster Carr) was applied to cover the lens of the objective in order to prevent direct contact with electrolyte. The wavelength of the laser excitation source was 532 nm with a laser power of ~0.5 mW at a grating of 1800 l mm^{-1}. Charge coupled device (CCD) detector was used to collect the scattered light from electrode surface. Prior to use, peak position of Raman spectrum was calibrated based on 520±0.5 cm^{-1} peak of silicon. Each spectrum was recorded with a resolution of ~1 cm^{-1} by setting up the measurement condition such that 30 consecutive scans and exposure time of 2 sec to laser at a beam spot were applied. All Raman experiments were carried out with a custom-made electrochemical cell in which a platinum wire and a custom-made double-junction Ag/AgCl served as counter and reference electrodes respectively. Prior to each experiment, the cell was dipped in an acid bath to remove all traces of metals and other dirt, and subsequently it was rinsed with acetone, alcohol and distilled water. For FeOOH-NiOOH samples, they were pressed with a hydraulic machine at 5 tons to make them flat and thin enough to fit the electrochemical Raman cell. For other powder-type samples (LDHs), the same catalyst ink as used in electrochemical measurements was drop-casted on a thin Au foil and then dried. The catalyst deposited Au was employed for subsequent operando Raman spectroscopy experiments.

5.3 Electrochemical test conditions

FeOOH-NiOOH (geometric area: 0.2-0.3 cm^2) was directly used for electrochemical measurements. For NiFe LDH samples, the catalyst ink was prepared by mixing of 1 mL water, 0.25 mL isopropanol, 0.01 mL 5 wt% Nafion solution and 3 mg materials. The ink was sonicated for at least 2 h. Then 160 µL/cm^2 of the ink was uniformly loaded onto a carbon cloth electrode (CC, plasma treated, geometric area: 0.2-0.3 cm^2). The electrodes were dried in a 75 °C oven for 30 mins before measurements.

All of the electrochemical measurements in this study were independently repeated for at least three times. The electrochemical measurements were performed in a three-electrode electrochemical cell, in which Pt wire and Ag/AgCl electrode (saturated KCl, E(Ag/AgCl) = 0.197 V vs. NHE, normal hydrogen electrode) were used as counter and reference electrode, respectively. The working electrode and reference electrode were separated with counter electrode by a glass frit. All potentials were reported versus the reversible hydrogen electrode (RHE) unless otherwise specified. Before measurements, all of the electrolyte were calibrated the point of 0 V versus RHE by standard hydrogen saturation calibration experiments. A glassy carbon electrode drop-casted by Pt/C was used as the working electrode. After bubbling with hydrogen for 30 mins, the electrode was subjected to linear scan voltammetry (LSV, scan rate: 2 mV/s), in which the current of both hydrogen evolution and hydrogen oxidation could be observed. The cross-point is 0 V vs. RHE. Based on Eq. 3, the pH values of various electrolytes can be measured. The solution was stirred by a magnetic stirring bar in all of the electrochemical measurements. The polarization curves were recorded by LSV, and the scan rate was 1 mV/s, with 95% IR correction. The data was collected from cathodic potential to anodic potential (forward scan). 3 LSV scans were obtained for each measurements and the third LSV was used for analysis. The first LSV was typically influenced by oxidative peak. The Tafel plots were derived from LSVs. To investigate redox peaks, the scan rate was set to 10 mV/s, with 90% IR correction. The activation process is performed from 1.20-1.53 V vs. RHE. The scan rate is 10 mV/s, with 90% IR correction. The TOFs were calculated by Eq. 4, where J is the anodic current density at certain overpotential, A is the geometrical surface area of the electrode, F is the Faraday constant (96485 C/mol), and m is the loadings of Fe (assumed to be active sites).

$$E(RHE) = E(Ag/AgCl) + 0.197 \text{ V} + 0.0592 \times pH \text{ V} \quad \text{(Eq. 3)}$$

$$TOF = \frac{J \times A}{4 \times F \times m} \quad \text{(Eq. 4)}$$

Electrochemical active surface area (ECSA) was calculated from double-layer capacitance (eq 5).[58] The C_s the specific capacitance of monolayer

$NiFeO_x$ (0.081 mF/cm^2),[59] while the C_{dl} are the double-layer capacitance of the working electrodes. The C_{dl} was measured according to eq 6, where j_a and j_c are charging and discharging current densities and υ is the scan rate. The potential range of the measurements is from 1.00 to 1.10 V vs. RHE, where no catalytic current and Ni redox peaks were observed. The difference of charging and discharging current densities at 1.05 V was used for calculation. The scan rates were from 10 to 200 mV/s (10, 20, 50, 100, 150, and 200 mV/s).

$$ECSA = \frac{C_{dl}}{C_s} \tag{Eq. 5}$$

$$C_{dl} = \frac{|j_a - j_c|}{2\upsilon} \tag{Eq. 6}$$

Electrokinetic studies were performed in KOH with concentration from 0.5 M – 2 M. The 0.5 M and 0.75 M KOH were prepared by dilute 1 M KOH standard solution, while 1.5 M and 2 M KOH were prepared by further adding desired amount of KOH flakes in 1 M KOH standard solution. The LSVs of investigated electrodes were obtained sequentially in 0.5 M, 0.75 M, 1 M, 1.5 M and 2 M KOH. The Tafel plots were derived from LSVs and linear fitted, as $(\partial E/\partial j)_{pH}$. The relationship between the potential at a constant current and the concentration of hydroxyl ions $((\partial E/\partial \log[OH^-])_j)$ were obtained by calculating the potential at a constant current (10 mA/cm^2 for FeOOH-NiOOH; 1 mA/cm^2 for NiFe LDH) and log [OH$^-$], and then linear fitting. The order dependence on the hydroxyl ions $((\partial j/\partial \log[OH^-])_E)$ in 0.5-2 M KOH can be determined according to Eq. 1. This parameter should not be directly read from LSVs since it is hard to ensure that in a certain potential, all the current densities are in Tafel region for KOH with different concentrations.

Cation effect of each catalysts was investigated in 1 M KOH, 1 M NaOH and 1 M LiOH. The point of 0 V vs. RHE of each electrolyte was calibrated by standard hydrogen saturation calibration method (see experimental section above). Noted that the apparent pH value of KOH, NaOH, LiOH is different, despite the same concentration. The pH values are 13.7, 13.5, 13.1 for 1 M KOH, NaOH, LiOH, respectively. The LSVs of investigated electrodes were obtained sequentially in 1 M KOH, 1 M NaOH and 1 M LiOH.

H/D isotope experiments were performed in 0.5 M and 1 M electrolyte. KOD in D_2O solution were prepared by diluting 30% KOD with D_2O to desired concentrations. The pH of KOH was calibrated by standard hydrogen saturation calibration method. The pD of KOD were calculated by adding 0.87 based on pH of KOH with same concentration. This treatment is according to the different pK_w values of H_2O (14.00) and D_2O (14.87). The isotope effect value is calculated by the ratio of the current density in KOH and KOD, in the same overpotential (Eq. 7). Noted that the theoretical potential of OER in water is 1.229 V vs. RHE, while that of OER in D_2O is 1.262 V vs. RDE (reversible deuterium electrode).[50] Therefore, the overpotential in KOH and in KOD is calculated as Eq. 8-9.

$$Isotope\ effect\ value = \frac{j_{KOH}}{j_{KOD}} \tag{Eq. 7}$$

$$\eta_{KOH} = E(Ag/AgCl) + 0.197\ V + 0.0592\ V \times pH - 1.229\ V \tag{Eq. 8}$$

$$\eta_{KOD} = E(Ag/AgCl) + 0.197\ V + 0.0592\ V \times (pH + 0.87) - 1.262\ V \tag{Eq. 9}$$

ASSOCIATED CONTENT

Supporting Information. The supporting information contains complementary data of TEM, operando Raman spectroscopies, electrokinetic analysis and model. This material is available free of charge via the Internet at http://pubs.acs.org.

AUTHOR INFORMATION

Corresponding Author

* Xile Hu − Laboratory of Inorganic Synthesis and Catalysis, Institute of Chemical Sciences and Engineering, École Polytechnique Fédérale de Lausanne (EPFL), ISIC-LSCI, 1015 Lausanne, Switzerland; Email: xile.hu@epfl.ch.

Author Contributions

‡These authors contributed equally.

REFERENCES

1. Lewis, N. S., Research opportunities to advance solar energy utilization. *Science* **2016,** *351*, aad1920.

2. Seh, Z. W.; Kibsgaard, J.; Dickens, C. F.; Chorkendorff, I.; Nørskov, J. K.; Jaramillo, T. F., Combining theory and experiment in electrocatalysis: Insights into materials design. *Science* **2017,** *355*, eaad4998.

3. Song, F.; Bai, L.; Moysiadou, A.; Lee, S.; Hu, C.; Liardet, L.; Hu, X., Transition Metal Oxides as Electrocatalysts for the Oxygen Evolution Reaction in Alkaline Solutions: An Application-Inspired Renaissance. *J Am Chem Soc* **2018,** *140*, 7748-7759.

4. Hunter, B. M.; Gray, H. B.; Muller, A. M., Earth-Abundant Heterogeneous Water Oxidation Catalysts. *Chem Rev* **2016,** *116*, 14120-14136.

5. Suen, N. T.; Hung, S. F.; Quan, Q.; Zhang, N.; Xu, Y. J.; Chen, H. M., Electrocatalysis for the oxygen evolution reaction: recent development and future perspectives. *Chem Soc Rev* **2017,** *46*, 337-365.

6. Dau, H.; Limberg, C.; Reier, T.; Risch, M.; Roggan, S.; Strasser, P., The Mechanism of Water Oxidation: From Electrolysis via Homogeneous to Biological Catalysis. *ChemCatChem* **2010,** *2*, 724-761.

7. Hu, C.; Zhang, L.; Gong, J., Recent progress made in the mechanism comprehension and design of electrocatalysts for alkaline water splitting. *Energy Environ Sci* **2019,** *12*, 2620-2645.

8. Man, I. C.; Su, H.-Y.; Calle-Vallejo, F.; Hansen, H. A.; Martínez, J. I.; Inoglu, N. G.; Kitchin, J.; Jaramillo, T. F.; Nørskov, J. K.; Rossmeisl, J., Universality in Oxygen Evolution Electrocatalysis on Oxide Surfaces. *ChemCatChem* **2011,** *3*, 1159-1165.

9. Koper, M. T. M., Thermodynamic theory of multi-electron transfer reactions: Implications for electrocatalysis. *J Electroanal Chem* **2011,** *660*, 254-260.

10. Busch, M., Water oxidation: From mechanisms to limitations. *Curr Opin Electrochem* **2018,** *9*, 278-284.

11. Busch, M.; Halck, N. B.; Kramm, U. I.; Siahrostami, S.; Krtil, P.; Rossmeisl, J., Beyond the top of the volcano? – A unified approach to electrocatalytic oxygen reduction and oxygen evolution. *Nano Energy* **2016,** *29*, 126-135.

12. Bajdich, M.; Garcia-Mota, M.; Vojvodic, A.; Norskov, J. K.; Bell, A. T., Theoretical investigation of the activity of cobalt oxides for the electrochemical oxidation of water. *J Am Chem Soc* **2013,** *135*, 13521-13530.

13. Wang, L.-P.; Van Voorhis, T., Direct-Coupling O2 Bond Forming a Pathway in Cobalt Oxide Water Oxidation Catalysts. *J Phy Chem Lett* **2011,** *2*, 2200-2204.

14. Bediako, D. K.; Surendranath, Y.; Nocera, D. G., Mechanistic studies of the oxygen evolution reaction mediated by a nickel-borate thin film electrocatalyst. *J Am Chem Soc* **2013,** *135*, 3662-3674.

15. Moysiadou, A.; Lee, S.; Hsu, C. S.; Chen, H. M.; Hu, X., Mechanism of Oxygen Evolution Catalyzed by Cobalt Oxyhydroxide:

Cobalt Superoxide Species as a Key Intermediate and Dioxygen Release as a Rate-Determining Step. *J Am Chem Soc* **2020,** *142*, 11901-11914.

16.   Surendranath, Y.; Kanan, M. W.; Nocera, D. G., Mechanistic studies of the oxygen evolution reaction by a cobalt-phosphate catalyst at neutral pH. *J Am Chem Soc* **2010,** *132*, 16501-16509.

17.   Halck, N. B.; Petrykin, V.; Krtil, P.; Rossmeisl, J., Beyond the volcano limitations in electrocatalysis--oxygen evolution reaction. *Phys Chem Chem Phys* **2014,** *16*, 13682-13688.

18.   Martirez, J. M. P.; Carter, E. A., Unraveling Oxygen Evolution on Iron-Doped beta-Nickel Oxyhydroxide: The Key Role of Highly Active Molecular-like Sites. *J Am Chem Soc* **2019,** *141*, 693-705.

19.   Song, F.; Busch, M. M.; Lassalle-Kaiser, B.; Hsu, C.-S.; Petkucheva, E.; Bensimon, M.; Chen, H. M.; Corminboeuf, C.; Hu, X., An Unconventional Iron Nickel Catalyst for the Oxygen Evolution Reaction. *ACS Cent. Sci.* **2019,** *5*, 558-568.

20.   Trotochaud, L.; Young, S. L.; Ranney, J. K.; Boettcher, S. W., Nickel-iron oxyhydroxide oxygen-evolution electrocatalysts: the role of intentional and incidental iron incorporation. *J Am Chem Soc* **2014,** *136*, 6744-6753.

21.   Stevens, M. B.; Trang, C. D. M.; Enman, L. J.; Deng, J.; Boettcher, S. W., Reactive Fe-Sites in Ni/Fe (Oxy)hydroxide Are Responsible for Exceptional Oxygen Electrocatalysis Activity. *J Am Chem Soc* **2017,** *139*, 11361-11364.

22.   Klaus, S.; Cai, Y.; Louie, M. W.; Trotochaud, L.; Bell, A. T., Effects of Fe Electrolyte Impurities on Ni(OH)2/NiOOH Structure and Oxygen Evolution Activity. *J Phy Chem C* **2015,** *119*, 7243-7254.

23.   Friebel, D.; Louie, M. W.; Bajdich, M.; Sanwald, K. E.; Cai, Y.; Wise, A. M.; Cheng, M. J.; Sokaras, D.; Weng, T. C.; Alonso-Mori, R.; Davis, R. C.; Bargar, J. R.; Norskov, J. K.; Nilsson, A.; Bell, A. T., Identification of highly active Fe sites in (Ni,Fe)OOH for electrocatalytic water splitting. *J Am Chem Soc* **2015,** *137*, 1305-1313.

24.   Diaz-Morales, O.; Ledezma-Yanez, I.; Koper, M. T. M.; Calle-Vallejo, F., Guidelines for the Rational Design of Ni-Based Double Hydroxide Electrocatalysts for the Oxygen Evolution Reaction. *ACS Catal* **2015,** *5*, 5380-5387.

25.   Li, Y.-F.; Selloni, A., Mechanism and Activity of Water Oxidation on Selected Surfaces of Pure and Fe-Doped NiOx. *ACS Catal* **2014,** *4*, 1148-1153.

26.   Xu, X.; Song, F.; Hu, X., A nickel iron diselenide-derived efficient oxygen-evolution catalyst. *Nat Commun* **2016,** *7*, 12324.

27.   Fu, D.; Keech, P. G.; Sun, X.; Wren, J. C., Iron oxyhydroxide nanoparticles formed by forced hydrolysis: dependence of phase composition on solution concentration. *Phys Chem Chem Phys* **2011,** *13*, 18523-18529.

28.   Francas, L.; Corby, S.; Selim, S.; Lee, D.; Mesa, C. A.; Godin, R.; Pastor, E.; Stephens, I. E. L.; Choi, K. S.; Durrant, J. R., Spectroelectrochemical study of water oxidation on nickel and iron oxyhydroxide electrocatalysts. *Nat Commun* **2019,** *10*, 5208.

29.   Stern, L. A.; Hu, X., Enhanced oxygen evolution activity by NiOx and Ni(OH)2 nanoparticles. *Faraday discussions* **2014,** *176*, 363-379.

30.   Chen, J.; Zheng, F.; Zhang, S.-J.; Fisher, A.; Zhou, Y.; Wang, Z.; Li, Y.; Xu, B.-B.; Li, J.-T.; Sun, S.-G., Interfacial Interaction between FeOOH and Ni–Fe LDH to Modulate the Local Electronic Structure for Enhanced OER Electrocatalysis. *ACS Catal* **2018,** *8*, 11342-11351.

31.   Yin, H.; Jiang, L.; Liu, P.; Al-Mamun, M.; Wang, Y.; Zhong, Y. L.; Yang, H.; Wang, D.; Tang, Z.; Zhao, H., Remarkably enhanced water splitting activity of nickel foam due to simple immersion in a ferric nitrate solution. *Nano Research* **2018,** *11*, 3959-3971.

32.   Lee, S.; Bai, L.; Hu, X., Deciphering Iron-Dependent Activity in Oxygen Evolution Catalyzed by Nickel-Iron Layered Hydroxide. *Angew Chem Int Ed* **2020,** *59*, 8072-8077.

33.   Lee, S.; Banjac, K.; Lingenfelder, M.; Hu, X., Oxygen Isotope Labeling Experiments Reveal Different Reaction Sites for the Oxygen Evolution Reaction on Nickel and Nickel Iron Oxides. *Angew Chem Int Ed* **2019,** *58*, 10295-10299.

34.   Trzesniewski, B. J.; Diaz-Morales, O.; Vermaas, D. A.; Longo, A.; Bras, W.; Koper, M. T.; Smith, W. A., In Situ Observation of Active Oxygen Species in Fe-Containing Ni-Based Oxygen Evolution Catalysts: The Effect of pH on Electrochemical Activity. *J Am Chem Soc* **2015,** *137*, 15112-15121.

35.   Louie, M. W.; Bell, A. T., An investigation of thin-film Ni-Fe oxide catalysts for the electrochemical evolution of oxygen. *J Am Chem Soc* **2013,** *135*, 12329-12337.

36.   Diaz-Morales, O.; Ferrus-Suspedra, D.; Koper, M. T. M., The importance of nickel oxyhydroxide deprotonation on its activity towards electrochemical water oxidation. *Chem Sci* **2016,** *7*, 2639-2645.

37.   Lu, Z.; Xu, W.; Zhu, W.; Yang, Q.; Lei, X.; Liu, J.; Li, Y.; Sun, X.; Duan, X., Three-dimensional NiFe layered double hydroxide film for high-efficiency oxygen evolution reaction. *Chem Commun* **2014,** *50*, 6479-6482.

38.   Zou, S.; Burke, M. S.; Kast, M. G.; Fan, J.; Danilovic, N.; Boettcher, S. W., Fe (Oxy)hydroxide Oxygen Evolution Reaction Electrocatalysis: Intrinsic Activity and the Roles of Electrical Conductivity, Substrate, and Dissolution. *Chem Mater* **2015,** *27*, 8011-8020.

39.   Bockris, J. O. M., Kinetics of activation controlled consecutive electrochemical reactions: anodic evolution of oxygen. *J Chem Phy* **1956,** *24*, 817-827.

40.   Lyons, M. E. G.; Brandon, M. P., A comparative study of the oxygen evolution reaction on oxidised nickel, cobalt and iron electrodes in base. *J Electroanal Chem* **2010,** *641*, 119-130.

41.   Fang, Y.-H.; Liu, Z.-P., Tafel Kinetics of Electrocatalytic Reactions: From Experiment to First-Principles. *ACS Catal* **2014,** *4*, 4364-4376.

42.   Vrubel, H.; Moehl, T.; Gratzel, M.; Hu, X., Revealing and accelerating slow electron transport in amorphous molybdenum sulphide particles for hydrogen evolution reaction. *Chem Commun* **2013,** *49*, 8985-8987.

43.   Chung, D. Y.; Park, S.; Lopes, P. P.; Stamenkovic, V. R.; Sung, Y.-E.; Markovic, N. M.; Strmcnik, D., Electrokinetic Analysis of Poorly Conductive Electrocatalytic Materials. *ACS Catal* **2020,** *10*, 4990-4996.

44.   Garcia, A. C.; Touzalin, T.; Nieuwland, C.; Perini, N.; Koper, M. T. M., Enhancement of Oxygen Evolution Activity of Nickel Oxyhydroxide by Electrolyte Alkali Cations. *Angew Chem Int Ed* **2019,** *58*, 12999-13003.

45.   Michael, J. D.; Demeter, E. L.; Illes, S. M.; Fan, Q.; Boes, J. R.; Kitchin, J. R., Alkaline Electrolyte and Fe Impurity Effects on the Performance and Active-Phase Structure of NiOOH Thin Films for OER Catalysis Applications. *J Phy Chem C* **2015,** *119*, 11475-11481.

46.   Zaffran, J.; Stevens, M. B.; Trang, C. D. M.; Nagli, M.; Shehadeh, M.; Boettcher, S. W.; Caspary Toroker, M., Influence of Electrolyte Cations on Ni(Fe)OOH Catalyzed Oxygen Evolution Reaction. *Chem Mater* **2017,** *29*, 4761-4767.

47.   Parkin, G., Temperature-Dependent Transitions Between Normal and Inverse Isotope Effects Pertaining to the Interaction of H−H and C−H Bonds with Transition Metal Centers. *Acc Chem Res* **2009,** *42*, 315-325.

48.   Zhang, W.; Burgess, I. J., Kinetic isotope effects in proton coupled electron transfer. *J Electroanal Chem* **2012,** *668*, 66-72.

49.   Pasquini, C.; Zaharieva, I.; Gonzalez-Flores, D.; Chernev, P.; Mohammadi, M. R.; Guidoni, L.; Smith, R. D. L.; Dau, H., H/D Isotope Effects Reveal Factors Controlling Catalytic Activity in Co-Based Oxides for Water Oxidation. *J Am Chem Soc* **2019,** *141*, 2938-2948.

50. Sakaushi, K., Quantum electrocatalysts: theoretical picture, electrochemical kinetic isotope effect analysis, and conjecture to understand microscopic mechanisms. *Phys Chem Chem Phys* **2020,** *22*, 11219-11243.

51. Krishtalik, L. I., The mechanism of the proton transfer: an outline. *Biochimica et Biophysica Acta (BBA) - Bioenergetics* **2000,** *1458*, 6-27.

52. Gómez-Gallego, M.; Sierra, M. A., Kinetic Isotope Effects in the Study of Organometallic Reaction Mechanisms. *Chem Rev* **2011,** *111*, 4857-4963.

53. Zhang, Y.; Zhang, H.; Ji, H.; Ma, W.; Chen, C.; Zhao, J., Pivotal Role and Regulation of Proton Transfer in Water Oxidation on Hematite Photoanodes. *J Am Chem Soc* **2016,** *138*, 2705-2711.

54. Liu, Y.; McCrory, C. C. L., Modulating the mechanism of electrocatalytic CO2 reduction by cobalt phthalocyanine through polymer coordination and encapsulation. *Nat Commun* **2019,** *10*, 1683.

55. Li, W.; Li, F.; Yang, H.; Wu, X.; Zhang, P.; Shan, Y.; Sun, L., A bio-inspired coordination polymer as outstanding water oxidation catalyst via second coordination sphere engineering. *Nat Commun* **2019,** *10*, 5074.

56. Li, N.; Bediako, D. K.; Hadt, R. G.; Hayes, D.; Kempa, T. J.; von Cube, F.; Bell, D. C.; Chen, L. X.; Nocera, D. G., Influence of iron doping on tetravalent nickel content in catalytic oxygen evolving films. *Proc Natl Acad Sci USA* **2017,** *114*, 1486.

57. Xu, L.; Wang, Z.; Chen, X.; Qu, Z.; Li, F.; Yang, W., Ultrathin layered double hydroxide nanosheets with Ni(III) active species obtained by exfoliation for highly efficient ethanol electrooxidation. *Electrochim Acta* **2018,** *260*, 898-904.

58. McCrory, C. C.; Jung, S.; Peters, J. C.; Jaramillo, T. F., Benchmarking heterogeneous electrocatalysts for the oxygen evolution reaction. *J Am Chem Soc* **2013,** *135*, 16977-16987.

59. Batchellor, A. S.; Boettcher, S. W., Pulse-Electrodeposited Ni–Fe (Oxy)hydroxide Oxygen Evolution Electrocatalysts with High Geometric and Intrinsic Activities at Large Mass Loadings. *ACS Catal* **2015,** *5*, 6680-6689.

Table of contents (TOC)

NiOOH

FeOOH